Journal of Power Sources 196 (2011) 3026–3032

Contents lists available at ScienceDirect

Journal of Power Sources

journal homepage: www.elsevier.com/locate/jpowsour

Microstructural and electrochemical impedance study of nickel–$Ce_{0.9}Gd_{0.1}O_{1.95}$ anodes for solid oxide fuel cells fabricated by ultrasonic spray pyrolysis

Lin Liu [a], Gap-Yong Kim [a,*], Andrew C. Hillier [b], Abhijit Chandra [a]

[a] Department of Mechanical Engineering, Iowa State University, 2034 Black Engineering Building, Ames, IA 50011, USA
[b] Department of Chemical and Biological Engineering, Iowa State University, Ames, IA, USA

ARTICLE INFO

Article history:
Received 7 October 2010
Received in revised form
22 November 2010
Accepted 22 November 2010
Available online 26 November 2010

Keywords:
Solid oxide fuel cell
Spray pyrolysis
Microstructure
AC impedance

ABSTRACT

Optimization of the electrode microstructure in a solid oxide fuel cell (SOFC) is an important approach to performance enhancement. In this study, the relationship between the microstructure and electrochemical performance of an anode electrode fabricated by ultrasonic spray pyrolysis was investigated. Nickel–$Ce_{0.9}Gd_{0.1}O_{1.95}$ (Ni–CGO) anodes were deposited on a dense yttria stabilized zirconia (YSZ) substrate by ultrasonic spray pyrolysis, and the resulting microstructure was analyzed. Scanning electron microscope (SEM) examinations revealed the impact of deposition temperature and precursor solution concentration on anode morphology, particle size and porosity. The electrochemical performance of the anode was measured by electrochemical impedance spectroscopy (EIS) using a Ni–CGO/YSZ/Ni–CGO symmetrical cell. The deposited anode had a particle size and porosity in ranging between 1.5–17 μm and 21%–52%, respectively. The estimated volume-specific triple phase boundary (TPB) length increased from 1.37×10^{-3} μm μm^{-3} to 1.77×10^{-1} μm μm^{-3} as a result of decrease of the particle size and increase of the porosity. The corresponding area specific charge transfer resistance decreased from 5.45 ohm cm^2 to 0.61 ohm cm^2 and the activation energy decreased from 1.06 eV to 0.86 eV as the TPB length increased.

1. Introduction

Solid oxide fuel cells (SOFCs) are electrochemical energy conversion devices that directly convert a chemical fuel source into electrical power. Much attention has been focused on improving the performance of the SOFC electrodes [1–4]. One potential improvement is to increase the number of reaction sites on the electrodes. The electrochemical reactions are known to occur at triple phase boundary (TPB) sites, where the reactant gas phase comes into contact with the electronic conductor and ionic conductor [5]. Increasing the extent of TPBs in the electrode thereby can be used to increase the reaction sites and produce better electrochemical performance. Also, a highly porous electrode is required to efficiently supply fuel gas to the TPB sites. Therefore, designing and controlling the microstructure of the electrode is critical in improving cell performance [6–8].

Various techniques have been used to fabricate SOFC electrodes, including tape casting [9], screen printing [10], spin coating [11], tape calendaring [12], thermal plasma spraying [13], electrostatic spray deposition [14] and spray pyrolysis [15]. These method have been summarized and compared in our pervious paper [16]. Compared with other techniques, spray pyrolysis has the most potential capability to control the deposition microstructure because of the flexibility in processing parameters and their impact on film structure. Several types of spray pyrolysis methods have been investigated to fabricate electrode in SOFCs, such as electrostatic spray pyrolysis [14,17–19], gas pressurized spray pyrolysis [20–22] and ultrasonic spray pyrolysis [15,23–25]. However, none of the studies on ultrasonic spray pyrolysis investigated porosity of the deposited electrode, which can significantly influence the electrode performance [26]. It is generally considered that the electrode performance highly depends on its microstructure. Despite a wealth of electrochemical analysis and data on nickel–gadolinium-doped-ceria (Ni–CGO) electrode on YSZ electrolyte, only a few studies experimentally have demonstrated the enhancement of electrochemical performance that can be achieved by manipulating electrode microstructure, such as changing the deposited particle size and electrode porosity [22,25]. Also, it remains unclear how changing both the particle size and electrode porosity impacts electrode performance.

Electrochemical impedance spectroscopy (EIS) has been widely used for SOFC component performance evaluation and degradation diagnostics [27–29]. EIS allows direct observation of electrochemical cell properties and the ability to unambiguously separate the role of electrolyte resistance from electrode performance. In this study, ultrasonic spray pyrolysis was used to deposit

* Corresponding author. Tel.: +1 515 294 6938; fax: +1 515 294 3261.
E-mail address: gykim@iastate.edu (G.-Y. Kim).

0378-7753/$ – see front matter © 2010 Elsevier B.V. All rights reserved.
doi:10.1016/j.jpowsour.2010.11.117

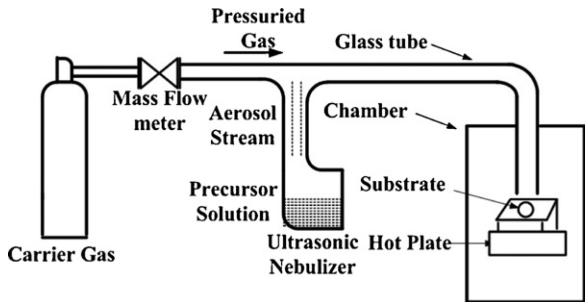

Fig. 1. Schematic of ultrasonic spray pyrolysis system.

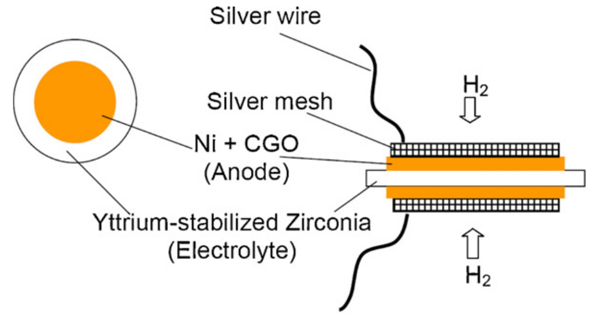

Fig. 2. Electrochemical impedance spectroscopy test configuration.

anode electrodes with varying particle size and porosity. EIS was then employed to measure the charge transfer resistance of the deposited anodes at various temperatures to quantitatively deduce the role of electrode microstructure on electrochemical activity.

2. Experimental procedure

The spray pyrolysis setup used in the electrode deposition is shown in Fig. 1. The setup consists of a carrier gas delivery system, a syringe pump, an ultrasonic nebulizer and a hot plate. The detailed description of the setup can be found in our earlier work [16]. In this study, 8 mol.% YSZ has been selected as the electrolyte material due to its wide use and affordability [30–32]. YSZ button cells (FCM®) were 20 mm in diameter and 270 μm in thickness with approximately 10% variation in thickness. Ni–CGO was selected as anode deposition material. Ni–CGO($Ce_{0.9}Gd_{0.1}O_{1.95}$) is considered as one of the state-of-the-art anode materials due to its high ionic conductivity, high electronic conductivity and high thermal and chemical stability, particularly in the presence of the YSZ electrolyte [17,33–40]. The precursor solution was prepared using a method similar to that described in [16]. Nickel (II) nitrate hexahydrate (98%, $N_2NiO_6{\cdot}6H_2O$; Alfa Aesar), cerium (III) nitrate hexahydrate (99.5%, $Ce(NO_3)_3{\cdot}6H_2O$; Alfa Aesar) and gadolinium (III) nitrate hydrate (99.9%, $Gd(NO_3)_3{\cdot}xH_2O$, $x \approx 6$; Alfa Aesar) were dissolved in the mixed organic solution of diethylene glycol mono-n-butyl ether (99%, $HOCH_2CH_2OCH_2CH_2O(CH_2)_3CH_3$; Alfa Aesar) and ethyl alcohol (99.5%, C_2H_5OH; Decon) at a volume ratio of 1:1. Then, the precursor solution was ultrasonically vibrated in a table top ultrasonic cleaner (Fisher FS 60H) for 30 min to make sure that powders completely dissolved into the solution. The molar ratio of Ni to CGO was chosen as 6:4 based on the research conducted by Chen and Hwang [25], which resulted in the best electrode performance in their study. Precursor solutions were prepared with different amounts of mixed organic solutions so that the total concentration of metal ions could be varied between 0.025 mol l^{-1} and 0.4 mol l^{-1}.

Two processing parameters were considered in this study: precursor solution concentration (C) and deposition temperature (T). Prior work showed that the precursor solution feed rate (L) had only a minor influence on the resulting film microstructure [16], and therefore, it was fixed at 1.23 ml min^{-1}. The full experiment matrix is provided in Table 1. The deposited samples were all annealed at 800 °C for 2 h to promote crystallization of the deposited film sat heat-up and cool-down rates of 5 °C min^{-1} under N_2 atmosphere. The morphology and composition of the deposited anode film were examined by scanning electron microscope (JEOL JSM-606LV) and energy dispersive X-ray spectrometer (INCA mics/x-stream/SEM TVA3). SEM images were analyzed by software, ImageJ, to calculate the deposition particle size and deposition film porosity. Siemens D-500 X-ray diffraction system was used to obtain the X-ray diffraction (XRD) pattern of the deposited samples.

Electrochemical impedance spectroscopy was carried out using a Ni–CGO/YSZ/Ni–CGO symmetrical cell (Fig. 2). The test samples were prepared using the conditions summarized in Table 2. All samples were reduced at 763 °C under H_2 environment for 90 min to fully facilitate the reduction of NiO before impedance testing. All measurements were recorded by an electrochemical workstation (CHI760, CH Instruments, Austin, TX) over the frequency range of 0.1Hz–100 kHz in a humidified H_2 environment. The temperature was varied between 663 °C and763 °C to investigate the effect of working electrode temperature on the anode performance for the different electrode microstructures. The measurement voltage amplitude was fixed at 10 mV. Silver wire (⌀0.5 mm, 99%, Sigma Aldrich) and silver current collecting mesh (Ag-M40-100, FCM®) were pasted on the anode surface to serve as a current collector.

3. Results and discussion

The ultrasonic spray pyrolysis method used in this study possesses the characteristics of both conventional spray pyrolysis and chemical vapor deposition (CVD). The deposition mecha-

Table 1
Experimental matrix used in the study.

Experiment #	1	2	3	4	5	6	7	8	9
Precursor solution concentration (mol l^{-1})	0.4	0.4	0.4	0.1	0.1	0.1	0.025	0.025	0.025
Deposition temperature (°C)	250	300	350	250	300	350	250	300	350

Precursor solution feed rate fixed as 1.23 ml min^{-1}.

Table 2
Test sample preparation condition and sample microstructure information.

#	Precursor solution concentration C (mol l^{-1})	Deposition temperature T (°C)	Average deposition particle size d_p (μm)	Deposited film porosity p (%)	Deposited film thickness (μm)
1	0.4	250	17	36	37
2	0.025	250	2.5	22	23
3	0.025	350	1.5	34	18

Precursor solution feed rate fixed as 1.23 ml min^{-1}.

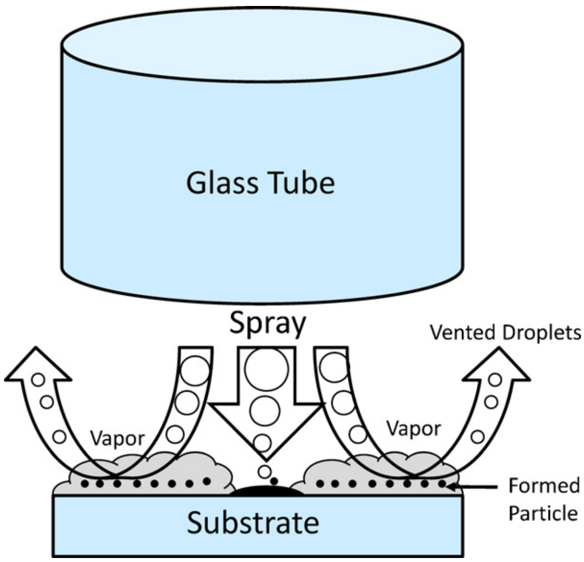

Fig. 3. Schematic of deposition mechanism of modified spray pyrolysis.

nism is schematically illustrated in Fig. 3. In conventional spray pyrolysis, the deposition occurs solely from high-velocity particles that strike the surface. In this approach, precursor aerosol is transported by a carrier gas, which enables deposition by evaporation–decomposition of precursor solution droplets. Therefore, the anode film is formed and thickened by the accumulation of droplets similar to that of aerosol assisted CVD [23,41,42]. Compared to conventional spray pyrolysis, the proposed method can deposit a more uniform film with uniformly-sized particles. It also effectively solves the dilemma of spray mist waste in the deposition area that occurs in conventional spray pyrolysis, which then requires spraying over a much larger area than the designed electrode to deposit a uniform film.

A typical microstructure of the deposited anode film is shown in Fig. 4. Composition analysis of this film is provided in Table 3, Figs. 5 and 6 Results indicate that Ni, Ce and Gd were present in the sample at a ratio of 15:8:1 (Table 3), which matches closely to the theoretically calculated value of 15:9:1 based on the molar ratio 6:4 of Ni and CGO. The weight ratio of NiO and CGO is about 50:50 without considering carbon, which comes from decomposition of the precursor solution. In addition, the deposited anode was analyzed by EDS mapping to reveal the spatial distribution of Ni, Ce and Gd in the sample. As shown in Figs. 5 and 6, the elements with corresponding diffraction pattern are homogenously distributed in the deposited film and within each particle. Thus, the proposed method is capable of fabricating anode composite film with well-dispersed constitutive elements.

The microstructures of the deposited anode were examined with SEM. Images of the microstructures obtained from the three different synthesis conditions are shown in to Fig. 7. A distinctly different electrode microstructure was observed for each. For Sample #1, perfectly spherical particles are observed, while larger necking between the particles was observed for Samples #2 and #3 due to sintering. Measured particle size and porosity are summarized in Table 2. The trend in particle size and porosity of the three samples is shown in Figs. 8 and 9, respectively. The particle size decreased from 17 μm in Sample #1 to 1.5–2.5 μm in Samples #2 and #3 by lowering the precursor solution concentration from 0.4 mol l^{-1} to 0.025 mol l^{-1}. Due to the effect of different deposition temperatures of Samples #2 and #3, the particle size slightly decreased slightly from 2.5 μm to 1.5 μm (see Fig. 9), and the deposited anode porosity increased from 22% to 34%. Discussion of the changes of porosity and deposition particle size were described in earlier work [16].

The electrochemical performance of the different anode structures was evaluated using EIS. Nyquist plots for the three samples at three different test temperatures are shown in Fig. 10. The impedance spectra were evaluated by fitting the impedance data with the equivalent circuit shown in Fig. 11. The equivalent circuit consists of an electrolyte resistance ($R_{electrolyte}$) in series with an

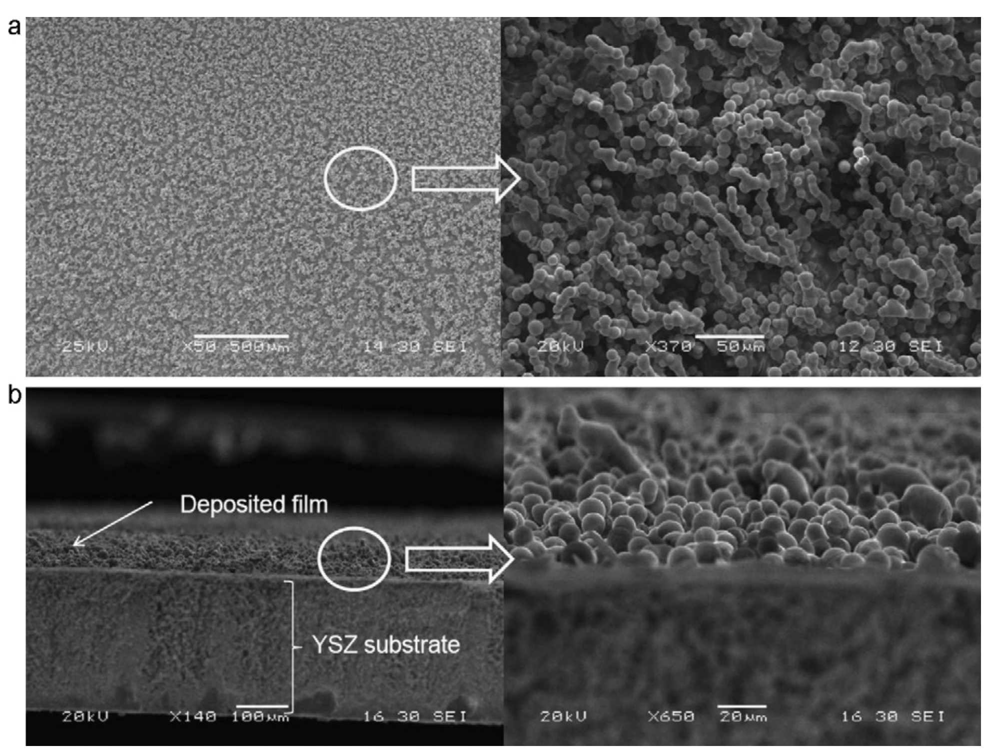

Fig. 4. Microstructure of deposited anode film (L = 1.23 ml min^{-1}, Q = 1.5 l min^{-1}, C = 0.1 mol l^{-1}, T = 300 °C): (a) top view and (b) cross section.

Table 3
EDS data showing element composition in the deposited anode film.

Element	App conc.	Intensity corrn.	Weight%	Weight% sigma	Atomic%
C	2.63	0.5533	4.75	0.41	14.38
O	31.82	1.2685	25.07	0.38	57.02
Ni	27.59	0.9434	29.22	0.37	18.11
Ce	33.39	0.9354	35.66	0.40	9.26
Gd	4.73	0.8923	5.30	0.33	1.23
Total			100.00		

electrode element consisting of a charge transfer resistance (R_{ct}) and a constant phase element (CPE). The CPE has an impedance $Z_{CPE} = 1/C(j\omega)\hat{}\alpha$, where $\alpha = 1$ reflects a perfect capacitance, while lower values can be the result of roughness or non-ideality in the electrode geometry. α values in the range of 0.53 ± 0.06 were used to successfully reproduce all the experimental results. Fitted curves for Sample #1 are provided in Fig. 10(a), which accurately captures the depressed semi-circles. The detailed mechanism and analysis on depressed arc can be found in the literature [43,44]. In the Nyquist plot, Z' and Z'' represent the real and imaginary values of the cell resistance as a function of the frequency. The interception of the impedance with the real axis Z′ in the low frequency regime corresponds to the total resistance, which includes the sum of the charge transfer and electrolyte resistances ($Z' = R_{electrolyte} + R_{ct}$). The intercept of the impedance with the real axis at the high frequency range reflects just the electrolyte resistance ($R_{electrolyte}$). Thus, the charge transfer resistance, which can be interpreted as being proportional to the electrochemical reaction rate at the anode electrode, can be determined by subtracting the electrolyte resistance from the total

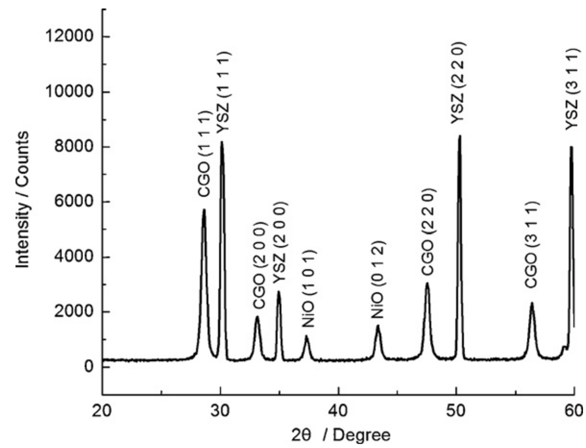

Fig. 6. XRD analysis of the deposited film.

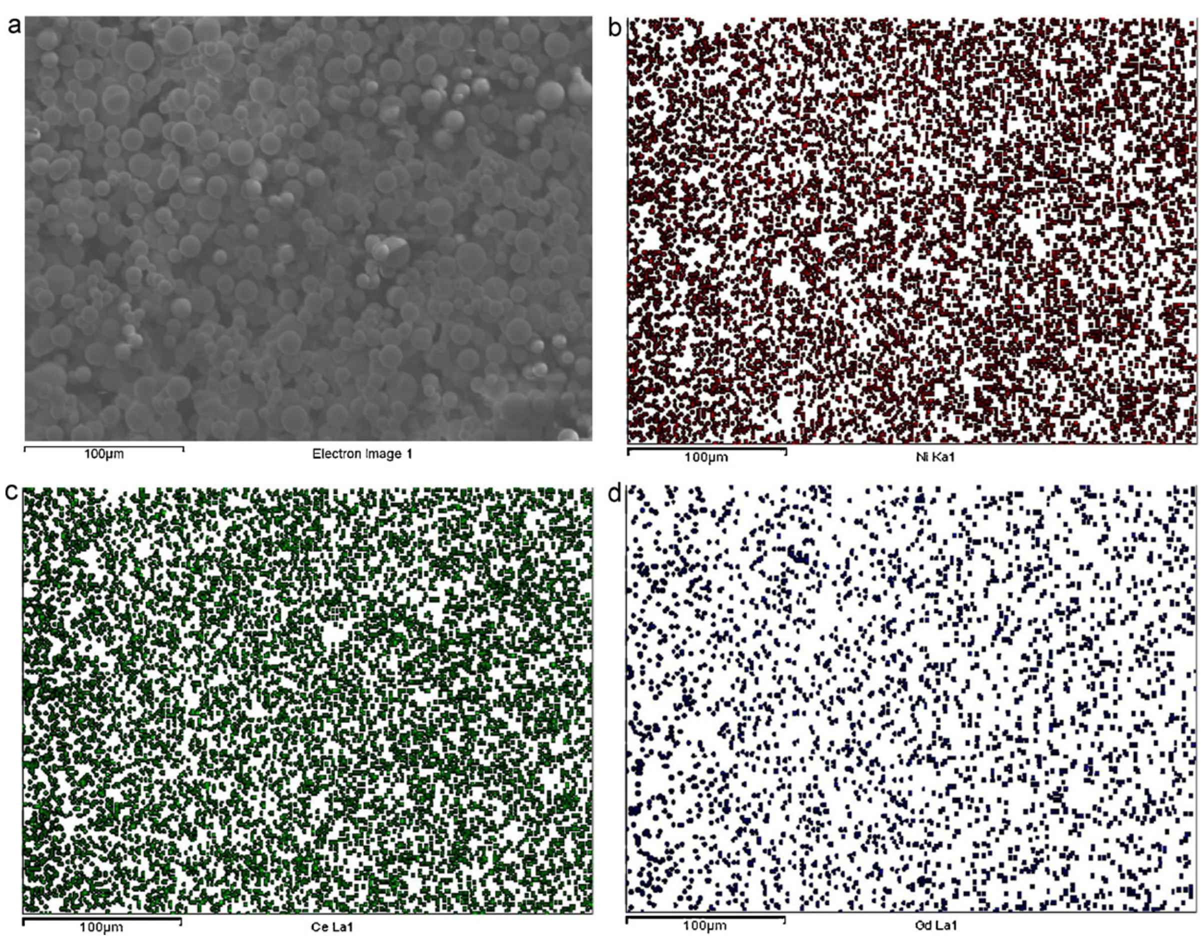

Fig. 5. SEM and EDS analysis of anode film: (a) SEM image of analyzed area, (b) nickel (c) cerium, and (d) gadolinium.

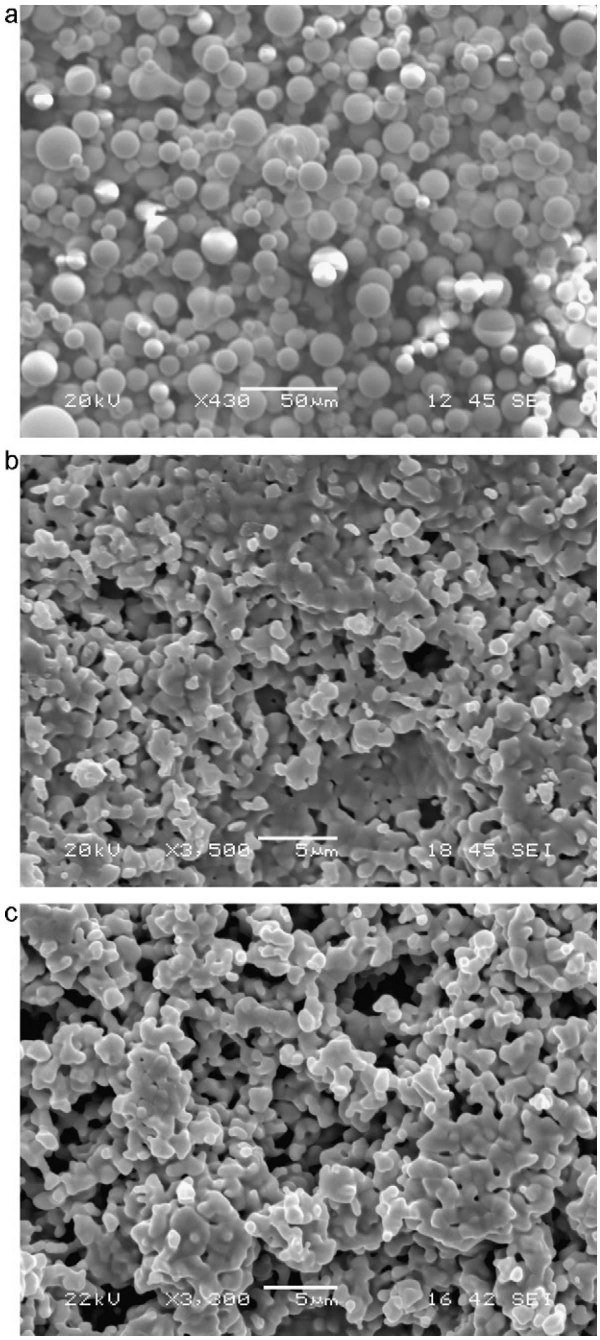

Fig. 7. SEM images of anode microstructures: (a) Sample #1 (d_p = 17 μm, p = 36%), (b) Sample #2 (d_p = 2.5 μm, p = 22%) and (c) Sample #3 (d_p = 1.5 μm, p = 34%).

cell resistance, which is also equal to the diameter of the impedance arc as measured at the intercept of the real axis.

The impedance results (Fig. 10) show a clear decrease in the charge transfer resistance with increasing temperature, as well as a decrease in charge transfer resistance among Samples #1, #2 and #3. Microstructural measurements show that Sample #3 has an order of magnitude smaller particle size than Sample #1. Prior research has shown that this decrease in particle size increases the TPBs and, thereby, improves the performance of deposited electrode [45]. This improvement in electrode performance is clearly seen here, where the charge transfer resistance also decreased by nearly an order of magnitude from 5.45 ohm cm^2 for Sample #1 to 0.61 ohm cm^2 for Sample #3 at 663 °C. Notably, these resistance values are within the typical range reported in the literature

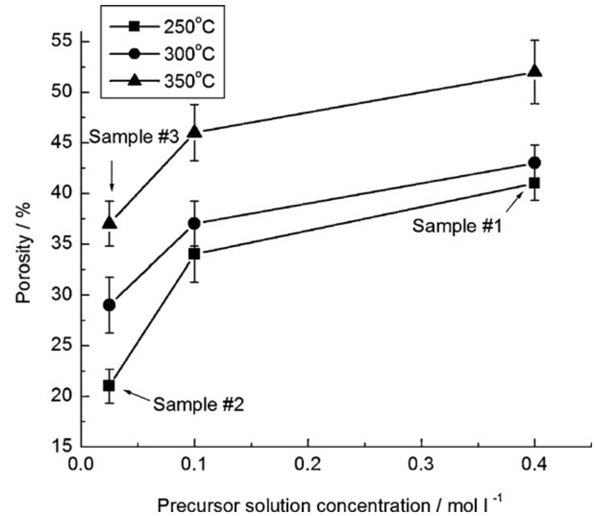

Fig. 8. Plot of film porosity versus temperature and precursor solution concentration (L = 1.23 ml min^{-1}, Q = 1.5 l min^{-1}).

[22,46,47]. Several factors may have contributed to the difference in the impedance values of Sample #2 (0.835 ohm cm^2) and Sample #3 (0.61 ohm cm^2). Slight differences in the particle size may be one factor. In addition, the decrease in the porosity for Sample #2 may have contributed to an increase in the charge transfer resistance over Sample #3. In the work performed by Chen and Hwang [25], impedance values were seen to increase with decreasing porosity of deposited electrode. Having a low porosity is likely to lead to mass transfer limitation. However, mass transfer limitation is expected to be very small for porosities above 20% [48].

The temperature dependent charge transfer resistances that were measures could be used to determine the activation energy (E_a) of the different electrodes. Notably, polarization resistance is closely associated with the amount of TPB, where the reactant gas (H_2) comes into contact with an electronic conductor (Ni) and an ionic conductor (CGO) providing continuing path for electrons and oxide ions. The activation energies (E_a) as determined from the impedance test are provided in the Arrhenius plot in Fig. 12 for the three different electrode samples. A decrease in the activation energy is observed when comparing Samples #1, #2 and #3.

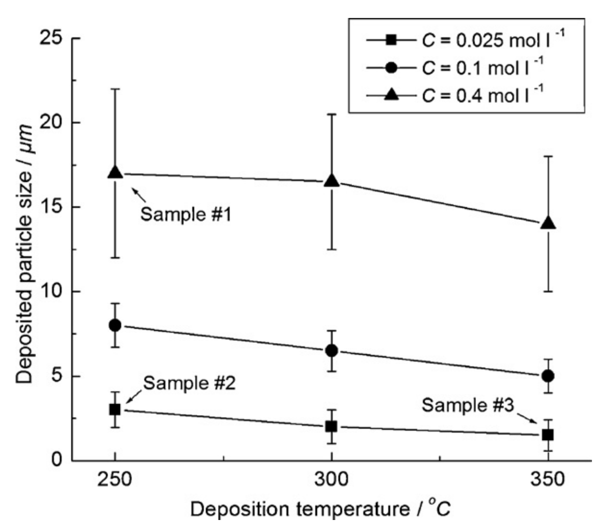

Fig. 9. Plot of particle size versus deposition temperature.

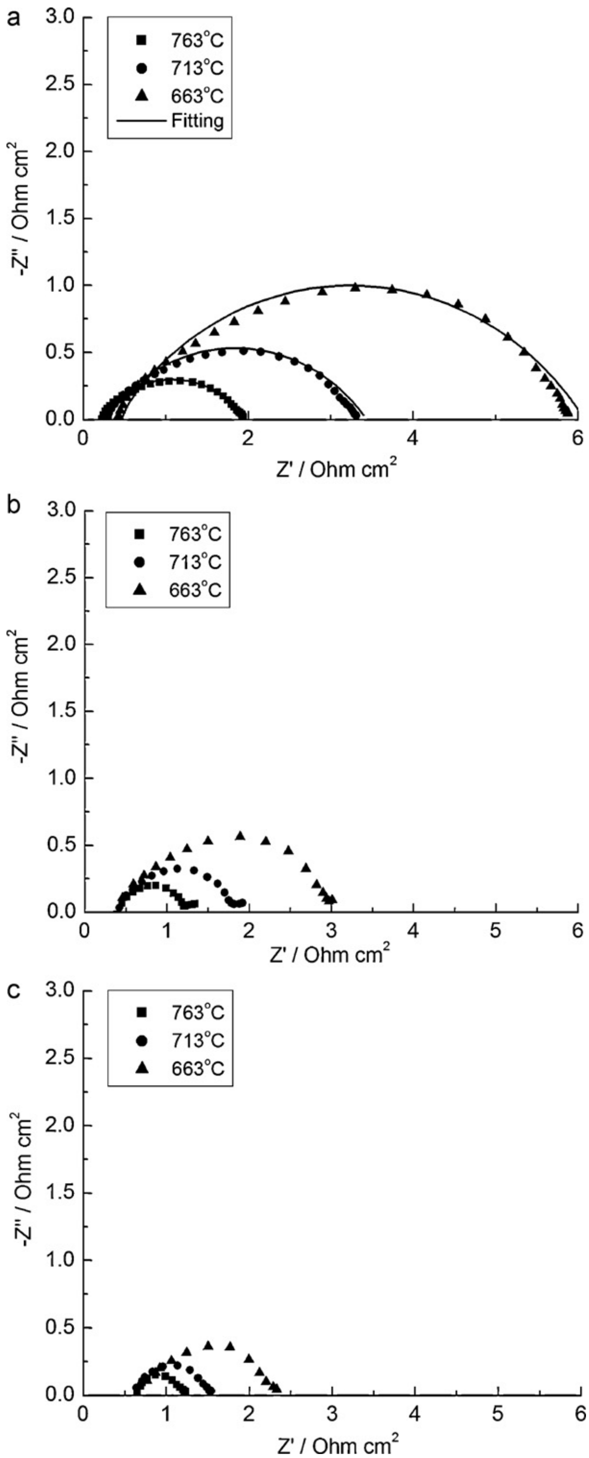

Fig. 10. Nyquist plots depicting EIS results for various samples at three test temperatures: (a) Sample #1 (d_p = 17 μm, p = 36%), (b) Sample #2 (d_p = 2.5 μm, p = 22%) and (c) Sample #3 (d_p = 1.5 μm, p = 34%).

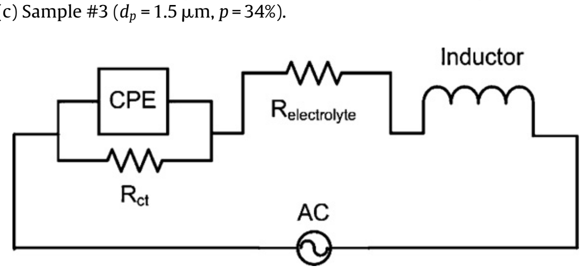

Fig. 11. Equivalent circuit of electrochemical test cell.

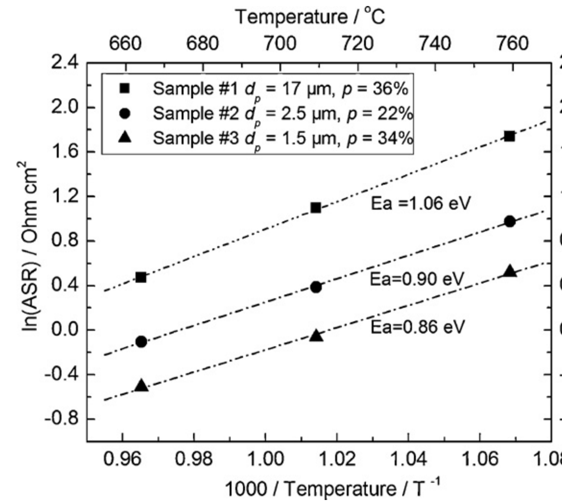

Fig. 12. Arrhenius plot of charge transfer resistances for three test samples.

The volume-specific TPB length was approximated by the following equation [49]:

$$L_{TPB} = \pi d_c N_t n_{io} n_{el} \frac{Z_{io} Z_{el}}{Z} P_{io} P_{el} \tag{1}$$

d_c is the diameter of necking connection between electronic conductor and ionic conductor. d_{el} is the diameter of electronic conductor, and d_{io} is the ionic conductor diameter. N_t (# μm^{-3}) is the number density of all particles. n_{el} and n_{io} are the number fractions of electronic conductor and ionic conductor. Z_{io} and Z_{el} are the coordination numbers for ionic and electronic conducting particles. Z is the average coordination number for random packing systems of spherical particles, which is 6 [49]. P_i is the probability of an i-phase particle to belong to the percolated clusters of the same phase [50,51]. The volume ratio of the electronic and ionic phases, which is related to the molar ratio used in this study, is taken into the TPB calculation through parameters n_{el}, n_{io}, Z_{el} and Z_{io}. The deposited particle size was estimated from the SEM images using ImageJ. It was assumed that the size of the ionic and electronic conducting particles was the same, and therefore, $d_{el} = d_{io} \approx 0.794 d_p$. The neck size can be approximated as $d_c \approx 0.26 d_{el}$ [52–57]. The calculated minimal L_{TPB} for Samples #1–#3 were 1.37×10^{-3} μm μm^{-3}, 9.65×10^{-2} μm μm^{-3} and 1.77×10^{-1} μm μm^{-3}, respectively. The parameters used for calculation are summarized in Table 4. Highest L_{TPB} were found in Sample #3, which contained the smallest particle size and largest porosity. As expected, microstructures with higher the L_{TPB} resulted in lower the area specific resistance (ARS). The activation energy was highest (E_a = 1.06 eV) in Sample #1 with largest particle size, and lower for smaller particle size electrodes (E_a = 0.90 and 0.86 eV). The values agree well with those reported in the literature [22,46]. For the porosity ranges produced by spray pyrolysis in this study (above 20%), particle size has a significant influence on the electrochemical performance of the electrode. However, if the particle size decreases to nanoscale, the effect of porosity may become a critical factor.

It can be observed that microstructures deposited by various processing conditions of spray pyrolysis result in different electrochemical performances. An effectively manipulated electrode microstructure can minimize activation and concentration polarizations [58]. Optimization of the electrode microstructure in a SOFC may be an important approach to cost reduction and reliability enhancement [27].

Table 4
Triple phase boundary length calculation parameter values.

Sample	d_p (μm)	p	N_t (# μm^{-3})	n_{el}	n_{io}	P_{el}	P_{io}
#1	17	0.36	4.976e−4	0.384	0.256	0.7469	0.5174
#2	2.5	0.22	1.907e−1	0.468	0.312	0.89	0.407
#3	1.5	0.34	7.471e−1	0.396	0.264	0.763	0.517

$Z_{el} = Z_{io} = 6$.

4. Conclusions

In this paper, a detailed experimental study was performed demonstrating an enhancement in electrode performance due to manipulation of the electrode microstructure. EDS and XRD analysis showed that all the elements of nickel, cerium and gadolinium, with corresponding diffraction patterns, were homogenously distributed on the substrate. This demonstrates the capability of ultrasonic spray pyrolysis to create highly dispersed films. The precursor solution concentration (0.025–0.4 mol l^{-1}) and deposition temperature (250 °C–350 °C) significantly influenced the deposited anode microstructure and resulted in changes of electrochemical performance. By manipulating these process parameters, the deposited particle size and porosity could be controlled in the range of 1.5–17 μm and 21–52%, respectively. The estimated volume-specific TPB length increased from 1.37×10^{-3} μm μm^{-3} to 1.77×10^{-1} μm μm^{-3} as a result of the decrease of the particle size and increase in porosity. Consistent with the estimated TPB length, the ASR of the anodes improved from 5.45 ohm cm^2 to 0.61 ohm cm^2, and the activation energy decreased from 1.06 eV to 0.86 eV for the temperature range of 663 °C to 763 °C. Ultimately, the influence of porosity on the electrode performance could not be independently isolated since the porosity of these films was above 20%, which is higher than typical mass transfer limited conditions.

This study demonstrated the potential of tailoring the electrode microstructure of a cell to improve the electrochemical performance of the SOFC using ultrasonic spray pyrolysis. In the future, this versatile fabrication technique will be utilized to study and design electrodes with varying microstructure and chemical composition to enhance the performance.

References

[1] S.P. Jiang, W. Wang, Y.D. Zhen, Journal of Power Sources 147 (2005) 1–7.
[2] S.P. Yoon, S.W. Nam, J. Han, T.H. Lim, S.A. Hong, S.H. Hyun, Solid State Ionics 166 (2004) 1–11.
[3] A. Ali, X. Wen, K. Nandakumar, J. Luo, K.T. Chuang, Journal of Power Sources 185 (2008) 961–966.
[4] H. Uchida, S. Arisaka, M. Watanabe, Solid State Ionics 135 (2000) 347–351.
[5] R. O'Hayre, D.M. Barnett, F.B. Prinz, Journal of the Electrochemical Society 152 (2005) A439–A444.
[6] C.W. Tanner, K.Z. Fung, A.V. Virkar, Journal of the Electrochemical Society 144 (1997) 21–30.
[7] J. Deseure, Y. Bultel, L. Dessemond, E. Siebert, Electrochimica Acta 50 (2005) 2037–2046.
[8] E.S. Greene, W.K.S. Chiu, M.G. Medeiros, Journal of Power Sources 161 (2006) 225–231.
[9] J.H. Song, S.I. Park, J.H. Lee, H.S. Kim, Journal of Materials Processing Technology 198 (2008) 414–418.
[10] D. Rotureau, J.P. Viricelle, C. Pijolat, N. Caillol, M. Pijolat, Journal of the European Ceramic Society 25 (2005) 2633–2636.
[11] X. Xu, C. Xia, S. Huang, D. Peng, Ceramics International 31 (2005) 1061–1064.
[12] N.Q. Minh, Solid State Ionics 174 (2004) 271–277.
[13] R. Hui, Z.W. Wang, O. Kesler, L. Rose, J. Jankovic, S. Yick, R. Maric, D. Ghosh, Journal of Power Sources 170 (2007) 308–323.
[14] T. Nguyen, E. Djurado, Solid State Ionics 138 (2001) 191–197.
[15] C.-L. Chang, C.-S. Hsu, B.-H. Hwang, Journal of Power Sources 179 (2008) 734–738.
[16] L. Liu, G.-Y. Kim, A. Chandra, J Power Sources 195 (2010) 7046–7053.
[17] Y. Xie, R. Neagu, C.-S. Hsu, X. Zhang, C. Deces-Petit, ECS Transactions 7 (2007) 787–794.
[18] O. Wilhelm, S.E. Pratsinis, D. Perednis, L.J. Gauckler, Thin Solid Films 479 (2005) 121–129.
[19] A. Princivalle, D. Perednis, R. Neagu, E. Djurado, Chemistry of Materials 16 (2004) 3733–3739.
[20] D. Beckel, A. Dubach, A. Studart, L. Gauckler, Journal of Electroceramics 16 (2006) 221–228.
[21] U.P. Muecke, G.L. Messing, L.J. Gauckler, Thin Solid Films 517 (2009) 1515–1521.
[22] U.P. Muecke, K. Akiba, A. Infortuna, T. Salkus, N.V. Stus, L.J. Gauckler, Solid State Ionics 178 (2008) 1762–1768.
[23] H.A. Hamedani, K.-H. Dahmen, D. Li, H. Peydaye-Saheli, H. Garmestani, M. Khaleel, Materials Science and Engineering: B 153 (2008) 1–9.
[24] K.K. Moe, T. Tagawa, S. Goto, Preparation of Electrode Catalyst for SOFC Reactor by Ultrasonic Mist Pyrolysis: Effect of Spray Time, Nippon seramikkusu kyokai, Tokyo, Japan, 1998.
[25] J.C. Chen, B.H. Hwang, Journal of the American Ceramic Society 91 (2008) 97–102.
[26] F. Zhao, A.V. Virkar, Journal of Power Sources 141 (2005) 79–95.
[27] Q.-A. Huang, R. Hui, B. Wang, J. Zhang, Electrochimica Acta 52 (2007) 8144–8164.
[28] A. Barbucci, M. Viviani, P. Carpanese, D. Vladikova, Z. Stoynov, Electrochimica Acta 51 (2006) 1641–1650.
[29] H. Koide, Y. Someya, T. Yoshida, T. Maruyama, Solid State Ionics 132 (2000) 253–260.
[30] K. Prabhakaran, M.O. Beigh, J. Lakra, N.M. Gokhale, S.C. Sharma, Journal of Materials Processing Technology 189 (2007) 178–181.
[31] H. Zhao, X. Li, F. Ju, U. Pal, Journal of Materials Processing Technology 200 (2008) 199–204.
[32] D. Simwonis, H. Thülen, F.J. Dias, A. Naoumidis, D. Stöver, Journal of Materials Processing Technology 92–93 (1999) 107–111.
[33] K. Chen, L. Zhe, N. Ai, X. Chen, J. Hu, X. Huang, W. Su, Journal of Power Sources 167 (2007) 84–89.
[34] J. Van herle, R. Ihringer, R. Vasquez Cavieres, L. Constantin, O. Bucheli, Journal of the European Ceramic Society 21 (2001) 1855–1859.
[35] M.G. Chourashiya, S.H. Pawar, L.D. Jadhav, Applied Surface Science 254 (2008) 3431–3435.
[36] M. Shi, N. Liu, Y.D. Xu, C. Wang, Y.P. Yuan, P. Majewski, F. Aldinger, Journal of Materials Processing Technology 169 (2005) 179–183.
[37] B.C.H. Steele, Solid State Ionics 129 (2000) 95–110.
[38] V.V. Kharton, F.M. Figueiredo, L. Navarro, E.N. Naumovich, A.V. Kovalevsky, A.A. Yaremchenko, A.P. Viskup, A. Carneiro, F.M.B. Marques, J.R. Frade, Journal of Material Science 36 (2001) 1105–1117.
[39] K. Higashinakagawa, S. Sameshima, Y. Hirata, Journal of Ceramic Processing Research 5 (2004) 84–88.
[40] S. Suda, M. Itagaki, E. Node, S. Takahashi, M. Kawano, H. Yoshida, T. Inagaki, Journal of the European Ceramic Society 26 (2006) 593–597.
[41] D. Perednis, L.J. Gauckler, Journal of Electroceramics 14 (2005) 103–111.
[42] K.L. Choy, B. Su, Thin Solid Films 388 (2001) 9–14.
[43] Y.J. Leng, S.H. Chan, K.A. Khor, S.P. Jiang, International Journal of Hydrogen Energy 29 (2004) 1025–1033.
[44] M. Makram, H. Mahmoud, B. Louati, F. Hlel, K. Guidara, Ionics 16 (2010) 655–660.
[45] C.-X. Li, C.-J. Li, L.-J. Guo, International Journal of Hydrogen Energy 35 (2010) 2964–2969.
[46] S. Primdahl, Y.L. Liu, Journal of The Electrochemical Society 149 (2002) A1466–A1472.
[47] T. Ishihara, T. Shibayama, H. Nishiguchi, Y. Takita, Solid State Ionics 132 (2000) 209–216.
[48] M.H. Abbasi, J.W. Evans, I.S. Abramson, AIChE Journal 29 (1983) 617–624.
[49] J.H. Nam, D.H. Jeon, Electrochimica Acta 51 (2006) 3446–3460.
[50] M. Suzuki, T. Oshima, Powder Technology 35 (1983) 159–166.
[51] D. Bouvard, F.F. Lange, Acta Metallurgica et Materialia 39 (1991) 3083–3090.
[52] P. Costamagna, P. Costa, V. Antonucci, Electrochimica Acta 43 (1998) 375–394.
[53] P. Costamagna, P. Costa, E. Arato, Electrochimica Acta 43 (1997) 967–972.
[54] P. Costamagna, M. Panizza, G. Cerisola, A. Barbucci, Electrochimica Acta 47 (2002) 1079–1089.
[55] S.H. Chan, Z.T. Xia, Journal of The Electrochemical Society 148 (2001) A388–A394.
[56] X.J. Chen, S.H. Chan, K.A. Khor, Electrochimica Acta 49 (2004) 1851–1861.
[57] S.H. Chan, X.J. Chen, K.A. Khor, Journal of The Electrochemical Society 151 (2004) A164–A172.
[58] A.V. Virkar, J. Chen, C.W. Tanner, J.W. Kim, Solid State Ionics 131 (2000) 189–198.